Frontiers of Information Technology & Electronic Engineering
www.jzus.zju.edu.cn; engineering.cae.cn; www.springerlink.com
ISSN 2095-9184 (print); ISSN 2095-9230 (online)
E-mail: jzus@zju.edu.cn

Efficient coherent detection of maneuvering targets based on location rotation transform and non-uniform fast Fourier transform*

Ke JIN[†‡1], Tao LAI[2], Yan-li QI[3], Jie HUANG[1], Yong-jun ZHAO[1]

[1]*National Digital Switching System Engineering and Technological Research Center, Zhengzhou 450001, China*

[2]*School of Electronics and Communication Engineering, Sun Yat-Sen University, Guangzhou 510000, China*

[3]*Anhui Institute of Quality and Standardization, Hefei 230000, China*

[†]E-mail: jinke_xd@outlook.com

Received May 29, 2019; Revision accepted July 17, 2019; Crosschecked July 14, 2020

Abstract: Long-term coherent integration can remarkably improve the ability of detection and motion parameter estimation of radar for maneuvering targets. However, the linear range migration, quadratic range migration (QRM), and Doppler frequency migration within the coherent processing interval seriously degrade the detection and estimation performance. Therefore, an efficient and noise-resistant coherent integration method based on location rotation transform (LRT) and non-uniform fast Fourier transform (NuFFT) is proposed. QRM is corrected by the second-order keystone transform. Using the relationship between the rotation angle and Doppler frequency, a novel phase compensation function is constructed. Motion parameters can be rapidly estimated by LRT and NuFFT. Compared with several representative algorithms, the proposed method achieves a nearly ideal detection performance with low computational cost. Finally, experiments based on measured radar data are conducted to verify the proposed algorithm.

Key words: Coherent integration; Maneuvering target; Parameter estimation; Location rotation transform (LRT); Non-uniform fast Fourier transform (NuFFT)

https://doi.org/10.1631/FITEE.1900272 **CLC number:** TN957.51

1 Introduction

Rapid advancements in stealth aircraft and unmanned aerial vehicles (UAVs) have placed increasing demands on radar detection for weak maneuvering targets (Su et al., 2010; Chen et al., 2014; Rao et al., 2014; Zhu SQ et al., 2014; Huang PH et al., 2016; Li et al., 2016c, 2016e; Jin et al., 2017; Wu et al., 2018). To detect such low radar cross section (RCS) targets, the first choice is the long-term coherent integration (Huang X et al., 2019; Li et al., 2019a, 2019b). Unfortunately, due to the high maneuverability of the targets, the effects of linear range migration (LRM), quadratic range migration (QRM), and Doppler frequency migration (DFM) will inevitably occur during the observation period (Xing et al., 2011; Tian et al., 2013, 2014). These unfavorable effects seriously deteriorate the detection performance of conventional integration methods, e.g., moving target detection (MTD). Consequently, finding ways to robustly detect weak maneuvering targets becomes a hot topic in the field of radar signal processing.

LRM makes a target's envelope move across range units after pulse compression. To eliminate the effects of LRM, many successful detection methods

‡ Corresponding author

* Project supported by the National Natural Science Foundation of China (No. 61501513)

ORCID: Ke JIN, https://orcid.org/0000-0003-4666-565X

© Zhejiang University and Springer-Verlag GmbH Germany, part of Springer Nature 2020

have been proposed, such as scaled inverse Fourier transform (SCIFT) (Zheng et al., 2015; Niu et al., 2017), keystone transform (KT) (Perry et al., 1999; Zhu DY et al., 2007; Pignol et al., 2018), modified location rotation transform (MLRT) (Sun et al., 2018), and Radon-Fourier transform (RFT) (Xu et al., 2011a, 2011b; Yu et al., 2012). These algorithms achieve satisfactory detection performances with reasonable computational cost. However, they may suffer from integration performance loss because they ignore the QRM and DFM caused by the target's acceleration.

Researchers have shown considerable interest in addressing these issues and developed many methods. In general, these methods can be roughly divided into two categories, i.e., search based algorithms and non-search algorithms. Search based algorithms include the generalized Radon-Fourier transform (GRFT) (Xu et al., 2012), KT and Lv's distribution (KT-LVD) (Lv et al., 2011; Luo et al., 2013; Li et al., 2016a), KT and linear canonical transform (KT-LCT) (Huang X et al., 2018), modified axis rotation transform and Lv's transform (MART-LVT) (Li et al., 2019a), improved axis rotation fractional Fourier transform (IAR-FRFT) (Rao et al., 2015), and Radon-Lv's distribution (RLVD) (Li et al., 2015). These methods can achieve superior detection performances at a low signal-to-noise ratio (SNR) by parameter search. However, high computational complexity makes them impractical in applications. Non-search algorithms include the symmetric autocorrelation function and scaled Fourier transform (SAF-SFT) (Li et al., 2018), three-dimensional scaled transform (TDST) (Zheng et al., 2018), frequency-domain second-order phase difference (FD-SoPD) (Jin et al., 2019a), and adjacent cross correlation function (ACCF) (Li et al., 2014, 2016d). These methods use correlation operations to reduce the coupling order, which greatly eases the computational burden. However, the nonlinear correlation brings cross terms of multiple targets and anti-noise performance loss (Jin et al., 2019b).

In this study, we continue our previous work (Jin et al., 2019a). To alleviate the competing interests of computational complexity and detection performance, an efficient and robust coherent detection method based on location rotation transform (LRT) and non-uniform fast Fourier transform (NuFFT), i.e., LRT-NuFFT, is proposed. First, the second-order keystone transform (SoKT) (Kirkland, 2011) is adopted to remove the effects of QRM. Then, using the relationship between the rotation angle and Doppler frequency, the effects of LRM and DFM are eliminated by LRT and NuFFT (Zheng et al., 2014; Qu et al., 2018). Comparison results of several representative methods show that the proposed method achieves a nearly ideal detection performance with low computational cost.

2 Signal model and problem formulation

Assume that a radar transmits a linear frequency-modulated signal as

$$s_T\left(\hat{t}\right)=\mathrm{rect}\left(\frac{\hat{t}}{T_\mathrm{p}}\right)\exp\left(\mathrm{j}2\pi f_\mathrm{c}\hat{t}+\mathrm{j}\pi\gamma\hat{t}^2\right) \tag{1}$$

with

$$\mathrm{rect}\left(\frac{\hat{t}}{T_\mathrm{p}}\right)=\begin{cases}1, & \left|\hat{t}\right|\le T_\mathrm{p}/2,\\ 0, & \left|\hat{t}\right|>T_\mathrm{p}/2,\end{cases}$$

where T_p is the pulse duration, f_c the carrier frequency, $\hat{t}$ the fast time variable, and γ the chirp rate.

Suppose that there is a maneuvering target moving with a constant acceleration, of which the instantaneous slant range $R(t_m)$ satisfies

$$R(t_m)=R_0+vt_m+\frac{1}{2}at_m^2, \tag{2}$$

where R_0, v, and a are the initial slant range, radial velocity, and acceleration of the target, respectively, and $t_m=mT$ (m=1, 2, …, N_a) the slow time variable (T is the pulse repetition time and N_a the number of integrated pulses).

Ignoring the influence of noise, the signal received after pulse compression can be expressed as

$$s_\mathrm{c}\left(\hat{t},t_m\right)=A_\mathrm{c}\mathrm{sinc}\left\{B\left[\hat{t}-\frac{2R(t_m)}{c}\right]\right\}\exp\left[-\mathrm{j}\frac{4\pi f_\mathrm{c}R(t_m)}{c}\right], \tag{3}$$

where A_c and B denote the amplitude and bandwidth of the signal, respectively, f_c the carrier frequency, and c the light speed.

Substituting Eq. (2) into Eq. (3) yields

$$s_{\mathrm{c}}\left(\hat{t},t_m\right)=A_{\mathrm{c}}\,\mathrm{sinc}\left\{B\left[\hat{t}-\frac{2(R_0+vt_m+0.5at_m^2)}{c}\right]\right\}\cdot\exp\left(-\mathrm{j}4\pi\frac{R_0+vt_m+0.5at_m^2}{\lambda}\right),\tag{4}$$

where $\lambda=c/f_{\mathrm{c}}$ is the wavelength.

Due to radar's low pulse repetition frequency (PRF) and target's high speed, Doppler ambiguity often occurs. Therefore, the radial velocity of the target can be expressed as (Zhang et al., 2017)

$$v=N_{\mathrm{b}}v_{\mathrm{b}}+v_0,\tag{5}$$

where $v_{\mathrm{b}}=\lambda f_{\mathrm{b}}/2$ is the blind speed (f_{b} is the PRF), N_{b} the Doppler ambiguity integer of the target, and v_0 the ambiguous velocity satisfying $-v_{\mathrm{b}}/2\le v_0<v_{\mathrm{b}}/2$.

We usually have $\exp(-\mathrm{j}2\pi f_{\mathrm{c}}N_{\mathrm{b}}v_{\mathrm{b}}t_m/c)=1$. Thus, substituting Eq. (5) into Eq. (4), we obtain

$$s_{\mathrm{c}}\left(\hat{t},t_m\right)=A_{\mathrm{c}}\,\mathrm{sinc}\left\{B\left[\hat{t}-\frac{2(R_0+vt_m+0.5at_m^2)}{c}\right]\right\}\cdot\exp\left(-\mathrm{j}4\pi\frac{R_0+v_0t_m+0.5at_m^2}{\lambda}\right),\tag{6}$$

showing that the signal envelope changes nonlinearly over slow time. When the offset caused by the target's velocity during the observation exceeds the range resolution $\Delta r=c/(2B)$, LRM will occur. If the target is highly maneuvering (i.e., with a large acceleration), QRM could occur.

Performing the Fourier transform (FT) on Eq. (6) along the fast time axis, we have

$$s(f_{\mathrm{r}},t_m)=A_{\mathrm{f}}\,\mathrm{rect}\left(\frac{f_{\mathrm{r}}}{B}\right)\exp\left(-\mathrm{j}4\pi f_{\mathrm{r}}\frac{N_{\mathrm{b}}v_{\mathrm{b}}t_m}{c}\right)\cdot\exp\left[-\mathrm{j}4\pi(f_{\mathrm{r}}+f_{\mathrm{c}})\frac{R_0+v_0t_m+0.5at_m^2}{c}\right],\tag{7}$$

where f_{r} denotes the range frequency with respect to $\hat{t}$. Eq. (7) indicates that the coupling between f_{r} and t_m is the essential cause of LRM and QRM. The Doppler frequency of the target, f_{d0}, is defined as

$$f_{\mathrm{d0}}=\frac{2}{\lambda}\frac{\mathrm{d}(R_0+v_0t_m+0.5at_m^2)}{\mathrm{d}t_m}=\frac{2(v_0+at_m)}{\lambda}.\tag{8}$$

Due to the target's acceleration, the Doppler offset is $2at_m/\lambda$. When this value exceeds the Doppler resolution $1/(N_{\mathrm{a}}T)$, DFM happens and leads to energy dispersion in the Doppler domain. Therefore, to detect a maneuvering target with a low SNR, the effects of LRM, QRM, and DFM should be eliminated by an effective detection algorithm.

3 Principle of the proposed coherent integration method

3.1 QRM elimination via SoKT

Employ SoKT to eliminate the quadratic coupling caused by the target's acceleration, which rescales the slow time for each range frequency and can be expressed as

$$t_m=\left[f_{\mathrm{c}}/(f_{\mathrm{r}}+f_{\mathrm{c}})\right]^{1/2}t_{\mathrm{a}},\tag{9}$$

where t_{a} denotes the scaled slow time.

Inserting Eq. (9) into Eq. (7) yields

$$\begin{aligned}s_{\mathrm{SoKT}}\left(f_{\mathrm{r}},t_{\mathrm{a}}\right)=&A_{\mathrm{f}}\,\mathrm{rect}\left(\frac{f_{\mathrm{r}}}{B}\right)\exp\left(-\mathrm{j}2\pi\frac{at_{\mathrm{a}}^2}{\lambda}\right)\\&\cdot\exp\left(-\mathrm{j}4\pi\frac{(f_{\mathrm{r}}+f_{\mathrm{c}})R_0}{c}\right)\\&\cdot\exp\left[-\mathrm{j}4\pi\left(1+\frac{f_{\mathrm{r}}}{f_{\mathrm{c}}}\right)^{1/2}f_{\mathrm{c}}\frac{v_0t_{\mathrm{a}}}{c}\right]\\&\cdot\exp\left[-\mathrm{j}4\pi f_{\mathrm{r}}\frac{N_{\mathrm{b}}v_{\mathrm{b}}t_{\mathrm{a}}}{c}\left(\frac{f_{\mathrm{c}}}{f_{\mathrm{c}}+f_{\mathrm{r}}}\right)^{1/2}\right].\end{aligned}\tag{10}$$

For a narrowband radar system, the first-order Taylor series expansion is used, expressed as

$$\begin{cases}\dfrac{f_{\mathrm{c}}}{f_{\mathrm{c}}+f_{\mathrm{r}}}\approx 1,\\[2ex]\left(1+\dfrac{f_{\mathrm{r}}}{f_{\mathrm{c}}}\right)^{1/2}\approx 1+\dfrac{f_{\mathrm{r}}}{2f_{\mathrm{c}}}.\end{cases}\tag{11}$$

Thus, Eq. (10) can be simplified as

$$s_{\mathrm{SoKT}}(f_{\mathrm{r}},t_{\mathrm{a}})=A_{\mathrm{f}}\,\mathrm{rect}\left(\frac{f_{\mathrm{r}}}{B}\right)\exp\left(-\mathrm{j}4\pi f_{\mathrm{r}}\frac{R_0+V_{\mathrm{e}}t_{\mathrm{a}}}{c}\right)\cdot\exp\left(-\mathrm{j}4\pi\frac{R_0+v_0t_{\mathrm{a}}+0.5at_{\mathrm{a}}^2}{\lambda}\right),\tag{12}$$

where $V_{\mathrm{e}}=N_{\mathrm{b}}v_{\mathrm{b}}+v_0/2$ is called the equivalent velocity of the target.

Performing the inverse Fourier transform (IFT) on Eq. (12) along f_{r}, we have

$$s_{\mathrm{SoKT}}(r,t_{\mathrm{a}})=A_{\mathrm{c}}\,\mathrm{sinc}\left[\frac{2B}{c}(r-R_0-V_{\mathrm{e}}t_{\mathrm{a}})\right]\cdot\exp\left(-\mathrm{j}4\pi\frac{R_0+v_0t_{\mathrm{a}}+0.5at_{\mathrm{a}}^2}{\lambda}\right),\tag{13}$$

where $r=c\hat{t}/2$ represents the range variable corresponding to $\hat{t}$.

From Eqs. (12) and (13), it is easy to see that SoKT eliminates the quadratic coupling between f_{r} and t_m. Therefore, QRM caused by the target's acceleration is accordingly eliminated.

3.2 LRM elimination and parameter estimation

The residual LRM and DFM in Eq. (13) bring significant challenges for coherent integration. In this subsection, we propose a novel efficient elimination method by jointly employing LRT and NuFFT.

Note that $t_{\mathrm{a}}=t_m$ and $f_{\mathrm{s}}=KB$, where f_{s} is the sampling frequency and K the oversampling rate. Thus, we have $r=\rho n$ and $R_0=\rho n_{R_0}$, where $\rho=c/(2f_{\mathrm{s}})$ denotes the range cell and n and n_{R_0} the range cell indices of r and R_0, respectively. In this case, Eq. (13) can be rewritten in the (n, m) coordinate system as

$$s_{\mathrm{SoKT}}(n,m)=A_{\mathrm{c}}\,\mathrm{sinc}\left[\frac{1}{K}\left(n-n_{R_0}\right)-\frac{1}{\Delta r}V_{\mathrm{e}}mT\right]\cdot\exp\left(-\mathrm{j}2\pi\frac{c}{\lambda KB}n_{R_0}\right)\exp\left(-\mathrm{j}\frac{4\pi}{\lambda}v_0mT\right)\cdot\exp\left[-\mathrm{j}\frac{2\pi}{\lambda}a(mT)^2\right].\tag{14}$$

To compensate for the LRM caused by equivalent velocity, LRT is introduced to perform the location rotation as

$$\begin{bmatrix}m\\n\end{bmatrix}=\begin{bmatrix}1&0\\\tan\varphi&1\end{bmatrix}\begin{bmatrix}m'\\n'\end{bmatrix},\quad\varphi\in\left(-\frac{\pi}{2},\frac{\pi}{2}\right),\tag{15}$$

where $[m'\ n']^{\mathrm{T}}$ represents the coordinates after rotation and φ the rotation angle.

Substituting Eq. (15) into Eq. (14) yields

$$s_{\mathrm{rot}}(n',m')=A_{\mathrm{c}}\exp\left(-\mathrm{j}2\pi\frac{c}{\lambda KB}n_{R_0}\right)\cdot\exp\left(-\mathrm{j}\frac{4\pi}{\lambda}v_0m'T\right)\exp\left(-\mathrm{j}\frac{2\pi}{\lambda}a(m'T)^2\right)\cdot\mathrm{sinc}\left[\frac{1}{K}\left(n'-n_{R_0}\right)+m'\left(\frac{\tan\varphi}{K}-\frac{V_{\mathrm{e}}T}{\Delta r}\right)\right].\tag{16}$$

When $\tan\varphi=KV_{\mathrm{e}}T/\Delta r$ or equivalently $\varphi=\arctan(KV_{\mathrm{e}}T/\Delta r)$, LRM in Eq. (16) will be eliminated, i.e.,

$$s_{\mathrm{rot}}(n',m')=A_{\mathrm{c}}\,\mathrm{sinc}\left[\frac{1}{K}\left(n'-n_{R_0}\right)\right]\cdot\exp\left(-\mathrm{j}\frac{2\pi c}{\lambda KB}n_{R_0}\right)\exp\left(-\mathrm{j}\frac{4\pi}{\lambda}v_0m'T\right)\cdot\exp\left(-\mathrm{j}\frac{2\pi}{\lambda}a(m'T)^2\right).\tag{17}$$

As shown in Eq. (17), the target's energy is located in the same range cell. Then, we can extract the signal along the slow time. For a certain range cell, the extracted signal can be expressed as

$$s_{\mathrm{azi}}(m')=A_{\mathrm{azi}}\exp\left(-\mathrm{j}\frac{2\pi c}{\lambda KB}n_{R_0}\right)\cdot\exp\left(-\mathrm{j}\frac{4\pi}{\lambda}v_0m'T\right)\cdot\exp\left[-\mathrm{j}\frac{2\pi}{\lambda}a(m'T)^2\right],\tag{18}$$

where A_{azi} is the amplitude.

It is evident that $s_{\mathrm{azi}}(m')$ is a chirp signal with respect to the slow time $m'T$. In Li et al. (2019a), LVT was used to complete coherent integration and motion parameter estimation, with satisfactory performance in integration and anti-noise. However, high computational cost remains daunting.

From Eqs. (17) and (18), note that V_e, v_0, and v can be obtained simultaneously from the rotation angle, expressed as

$$\hat{V}_e = \Delta r \frac{\tan\varphi}{KT}, \tag{19}$$

where $\hat{V}_e$ is the estimate of V_e.

According to Eq. (12), v_0 can be estimated as

$$\hat{v}_0 = 2\left[\hat{V}_e - \text{round}\left(\frac{\hat{V}_e}{v_b}\right)\cdot v_b\right], \tag{20}$$

where round(·) denotes the round-up operation and $\text{round}\left(\hat{V}_e/v_b\right)$ is the estimated Doppler ambiguity integer of the target. Then, the target's velocity is estimated as

$$\hat{v} = \text{round}\left(\hat{V}_e/v_b\right)\cdot v_b + \hat{v}_0. \tag{21}$$

With the estimated $\hat{v}_0$, a novel phase compensation function is constructed as

$$H_1(m') = \exp\left(\text{j}\frac{4\pi}{\lambda}\hat{v}_0 m'T\right). \tag{22}$$

Multiplying Eq. (22) with Eq. (18), the linear phase term will be compensated for. Therefore, an efficient NuFFT can be performed to realize energy accumulation and parameter estimation, i.e.,

$$\begin{aligned} & s_{\text{NuFFT}}\left(f_{(m'T)^2}\right) \\ &= \text{NuFFT}\left(s_{\text{azi}}(m')H_1(m')\right) \\ &= \sum_{m'=-N_a/2}^{N_a/2-1} s_{\text{azi}}(m')H_1(m')\exp\left[-\text{j}2\pi f_{(m'T)^2}(m'T)^2\right] \\ &= A_{\text{NuFFT}}\exp\left(-\text{j}\frac{2\pi c}{\lambda KB}n_{R_0}\right)p\left(f_{(m'T)^2}+\frac{a}{\lambda}\right), \end{aligned} \tag{23}$$

where NuFFT(·) presents the NuFFT operation, $p(\cdot)$ the impulse response function of NuFFT, and $f_{(m'T)^2}$ the frequency variable corresponding to $(m'T)^2$.

According to Eq. (23), it is clear that the target's energy is concentrated into a single peak, whose location indicates the target's acceleration, i.e.,

$$\begin{cases} \hat{f}_{(m'T)^2} = \arg\max\limits_{f_{(m'T)^2}}\left\{\left|s_{\text{NuFFT}}\left(f_{(m'T)^2}\right)\right|\right\}, \\ \hat{a} = \lambda\hat{f}_{(m'T)^2}. \end{cases} \tag{24}$$

3.3 Coherent integration and target detection

With the estimated velocity and acceleration, another phase compensation function is constructed to compensate for the effects of LRM, QRM, and DFM, which can be written as

$$\begin{aligned} H_2(f_r,t_m) &= \exp\left(\text{j}4\pi f_r\frac{\hat{v}t_m + 0.5\hat{a}t_m^2}{c}\right) \\ &\cdot\exp\left(\text{j}4\pi f_c\frac{0.5\hat{a}t_m^2}{c}\right). \end{aligned} \tag{25}$$

Finally, long-term coherent integration is achieved via slow time FT and spatial frequency IFT with respect to Eq. (7), expressed as

$$\begin{aligned} s_{\text{CI}}\left(\hat{t},f_d\right) &= \text{FT}_{t_m}\left\{\text{IFT}_{f_r}\left[S(f_r,t_m)H_2(f_r,t_m)\right]\right\} \\ &= A_{\text{CI}}\,\text{sinc}\left[B\left(\hat{t}-\frac{2R_0}{c}\right)\right] \\ &\cdot\text{sinc}\left[N_aT\left(f_d+\frac{2v_0}{\lambda}\right)\right], \end{aligned} \tag{26}$$

where A_{CI} denotes the complex amplitude after coherent integration and f_d the Doppler frequency corresponding to t_m.

In Eq. (26), the received signal of a maneuvering target is integrated into a single peak at the position of $(2R_0/c,\ -2v_0/\lambda)$, and the peak value is $|s_{\text{CI}}(2R_0/c,\ -2v_0/\lambda)|$. Therefore, the constant false alarm rate (CFAR) (Guida et al., 1993) can be used for target detection, expressed as

$$\left|s_{\text{CI}}\left(\frac{2R_0}{c},\frac{-2v_0}{\lambda}\right)\right| \underset{H_0}{\overset{H_1}{\lessgtr}} \eta, \tag{27}$$

where η is the detection threshold. The adaptive threshold is obtained by the reference unit after coherent integration via the integration method. Then,

the test statistic in the detecting unit is compared with the threshold to confirm the presence or absence of a target (Li et al., 2016a). If the test statistic is smaller than the threshold, there is no moving target (or a target is missed); then, go on to the next detecting unit. Otherwise, if the test statistic is larger than the threshold, target detection is declared.

3.4 Detailed procedure of the LRT-NuFFT method

The detailed implementation procedure of the LRT-NuFFT method is summarized as follows:

Step 1: Perform pulse compression on the radar echoes and obtain $s_{\mathrm{c}}\left(\hat{t}, t_m\right)$.

Step 2: Perform SoKT to correct QRM and use range IFT to obtain $s_{\mathrm{SoKT}}(n, m)$.

Step 3: According to the interested scope of velocity, determine the rotation angle search scope $[\varphi_{\min}, \varphi_{\max}]$. The search interval $\Delta\varphi$ should be smaller than $\arctan[\lambda/(2N_{\mathrm{a}}\rho)]$.

Step 4: With a certain rotation angle, perform LRT on $s_{\mathrm{SoKT}}(n, m)$. Then we can obtain the signal after rotation $s_{\mathrm{rot}}(n', m')$.

Step 5: Construct the phase compensation function $H_1(m')$ according to the search rotation angle (Eqs. (19)–(22)), and extract the data along the slow time and obtain $s_{\mathrm{azi}}(m')$.

Step 6: Perform the NuFFT operation on $s_{\mathrm{azi}}(m')\cdot H_1(m')$ to realize target energy accumulation and acceleration estimation (Eq. (23)).

Step 7: When the initial range and search rotation angle match the target's true value, the output of NuFFT will reach its maximum value. Then, estimate the target's velocity and acceleration via Eqs. (21) and (24), respectively.

Step 8: Construct another phase compensation function $H_2(f_{\mathrm{r}}, t_m)$ with the estimated motion parameters and complete coherent integration via Eqs. (25) and (26).

The flowchart of the LRT-NuFFT method is shown in Fig. 1.

Remark 1 Compared with MART-LVT (Li et al., 2019a), improvements and advantages of LRT-NuFFT are as follows: (1) In MART-LVT, the QRM effects caused by the target's acceleration are neglected, which causes integration performance loss in some specific situations. However, SoKT is first used to correct QRM in LRT-NuFFT, which makes it better suited for detecting highly maneuvering targets. (2) Different from MART-LVT, the relationship between φ and v_0 is employed to construct a phase compensation function. Thus, the subsequent energy accumulation and acceleration estimation can be achieved via NuFFT, greatly alleviating the computational burden of LVD. Detailed computational complexity comparisons will be given in Section 4.3.

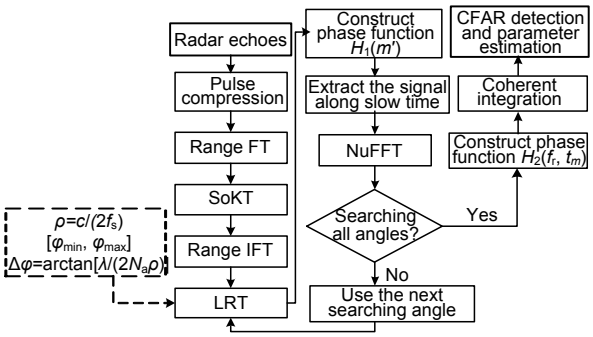

Fig. 1 Flowchart of the proposed method

4 Analysis of the proposed method

4.1 Multi-target analysis

Consider that Q targets are observed during the integration time. Similar to Eq. (14), the result of SoKT can be expressed as

$$\begin{aligned} & s_{\mathrm{SoKT}}(n,m) \\ &= \sum_{q=1}^{Q} A_{\mathrm{c},q} \exp\left(-\mathrm{j}\frac{2\pi c}{\lambda KB} n_{R_0,q}\right) \\ &\quad \cdot \exp\left(-\mathrm{j}\frac{4\pi}{\lambda} v_{0,q} mT\right) \exp\left[-\mathrm{j}\frac{2\pi}{\lambda} a_q (mT)^2\right] \\ &\quad \cdot \operatorname{sinc}\left[\frac{1}{K}\left(n - n_{R_0,q}\right) - \frac{1}{\Delta r} V_{\mathrm{e},q} mT\right]. \end{aligned} \tag{28}$$

Performing LRT on Eq. (28), we obtain

$$\begin{aligned} & s_{\mathrm{rot}}(n',m') \\ &= \sum_{q=1}^{Q} A_{\mathrm{c},q} \exp\left(-\mathrm{j}\frac{2\pi c}{\lambda KB} n_{R_0,q}\right) \\ &\quad \cdot \exp\left(-\mathrm{j}\frac{4\pi}{\lambda} v_{0,q} m'T\right) \exp\left[-\mathrm{j}\frac{2\pi}{\lambda} a_q (m'T)^2\right] \\ &\quad \cdot \operatorname{sinc}\left[\frac{1}{K}\left(n' - n_{R_0,q}\right) + m'\left(\frac{\tan\varphi}{K} - \frac{V_{\mathrm{e},q}T}{\Delta r}\right)\right]. \end{aligned} \tag{29}$$

When $\tan\varphi=KV_{\mathrm{e},i}T/\Delta r$, LRM of the ith target is corrected. However, LRM of other $(q-1)$ targets still exists, i.e.,

$$\begin{aligned}&s_{\mathrm{rot}}(n',m')\\&=A_{\mathrm{c},i}\exp\left(-\mathrm{j}\frac{2\pi c}{\lambda KB}n_{R_0,i}\right)\exp\left(-\mathrm{j}\frac{4\pi}{\lambda}v_{0,i}m'T\right)\\&\cdot\exp\left[-\mathrm{j}\frac{2\pi}{\lambda}a_i(m'T)^2\right]\mathrm{sinc}\left[\frac{1}{K}\left(n'-n_{R_0,i}\right)\right]\\&+\sum_{q=1,q\neq i}^{Q}A_{\mathrm{c},q}\exp\left(-\mathrm{j}\frac{2\pi c}{\lambda KB}n_{R_0,q}\right)\\&\cdot\exp\left(-\mathrm{j}\frac{4\pi}{\lambda}v_{0,q}m'T\right)\exp\left[-\mathrm{j}\frac{2\pi}{\lambda}a_q(m'T)^2\right]\\&\cdot\mathrm{sinc}\left[\frac{1}{K}\left(n'-n_{R_0,q}\right)+\frac{m'T}{\Delta r}\left(V_{\mathrm{e},i}-V_{\mathrm{e},q}\right)\right].\end{aligned}\tag{30}$$

Then, extract the signal along the slow time of range cell $n_{R_0,i}$, and we obtain

$$\begin{aligned}&s_{\mathrm{azi}}\left(m';n_{R_0,i}\right)\\&=A_{\mathrm{c},i}\exp\left(-\mathrm{j}\frac{2\pi c}{\lambda KB}n_{R_0,i}\right)\exp\left(-\mathrm{j}\frac{4\pi}{\lambda}v_{0,i}m'T\right)\\&\cdot\exp\left[-\mathrm{j}\frac{2\pi}{\lambda}a_i(m'T)^2\right]+s_{\mathrm{other}}\left(m';n_{R_0,i}\right),\end{aligned}\tag{31}$$

where

$$\begin{aligned}&s_{\mathrm{other}}\left(m';n_{R_0,i}\right)\\&=\sum_{q=1,q\neq i}^{Q}A_{\mathrm{c},q}\exp\left(-\mathrm{j}\frac{2\pi c}{\lambda KB}n_{R_0,q}\right)\\&\cdot\exp\left(-\mathrm{j}\frac{4\pi}{\lambda}v_{0,q}m'T\right)\exp\left(-\mathrm{j}\frac{2\pi}{\lambda}a_q(m'T)^2\right)\\&\cdot\mathrm{sinc}\left[\frac{1}{K}\left(n_{R_0,i}-n_{R_0,q}\right)+\frac{m'\mathrm{T}}{\Delta r}\left(V_{\mathrm{e},i}-V_{\mathrm{e},q}\right)\right].\end{aligned}\tag{32}$$

Similar to Eqs. (19)–(22), construct the phase compensation function according to the rotation angle, i.e.,

$$H_1(m')=\exp\left(\mathrm{j}\frac{4\pi}{\lambda}\hat{v}_{0,i}m'T\right).\tag{33}$$

Multiply Eq. (31) with Eq. (33), perform NuFFT to concentrate the target energy, and estimate the acceleration, so that we have

$$\begin{aligned}&s_{\mathrm{NuFFT}}\left(f_{(m'T)^2}\right)\\&=\mathrm{NuFFT}\left[s_{\mathrm{azi}}\left(m';n_{R_0,i}\right)H_1(m')\right]\\&=s_{\mathrm{nu},i}\left(f_{(m'T)^2}\right)+s_{\mathrm{other}}\left(f_{(m'T)^2}\right)\\&=A_{\mathrm{NuFFT},i}\exp\left(-\mathrm{j}\frac{2\pi c}{\lambda KB}n_{R_0,i}\right)p\left(f_{(m'T)^2}+\frac{a_i}{\lambda}\right)\\&\quad+s_{\mathrm{other}}\left(f_{(m'T)^2}\right).\end{aligned}\tag{34}$$

Note that only the ith target's energy is concentrated into a single peak, while other targets' energy is dispersed due to two reasons: the envelopes of other targets are distributed in different range cells and the linear phase term $\exp\left(-\mathrm{j}4\pi v_{0,q}m'T/\lambda\right)$ in Eq. (32) could not be well compensated for by $H_1(m')$.

Finally, the motion parameter estimation and coherent integration of the ith target can be achieved. However, other targets' energy will not be focused using the ith target's parameters.

Remark 2 Compared with MART-LVT, KT-LVD, TDST, SAF-SFT, and ACCF, LRT-NuFFT has no nonlinear operations. Thus, no cross terms appear, and the linearity property holds. Although LVD, TDST, SAF-SFT, and ACCF have satisfactory cross-term suppression ability, weak targets are still easily submerged in the residual cross-terms generated by strong targets.

4.2 Equivalent implementation via velocity search

The LRT-NuFFT method corrects LRM by searching for the rotation angle. However, the implementation of LRT requires extensive interpolation operations, which inevitably cause numerical errors. In addition, the rotation angle is not a natural representation of the target motion parameter. To solve this problem, we propose the equivalent interpolation-free implementation of LRT-NuFFT, namely, the velocity search NuFFT (VS-NuFFT) method.

Considering the LRT operation, Eq. (16) can be rewritten as

$$\begin{aligned} & s_{\mathrm{rot}}(n',m';V_{\mathrm{s}}) \\ &= A_{\mathrm{c}}\exp\left(-\mathrm{j}\frac{2\pi c}{\lambda KB}n_{R_0}\right) \\ &\quad\cdot\exp\left(-\mathrm{j}\frac{4\pi}{\lambda}v_0 m'T\right)\exp\left[-\mathrm{j}\frac{2\pi}{\lambda}a(m'T)^2\right] \\ &\quad\cdot\mathrm{sinc}\left[\frac{1}{K}\left(n'-n_{R_0}\right)+\frac{m'T}{\Delta r}(V_{\mathrm{s}}-V_{\mathrm{e}})\right], \end{aligned} \tag{35}$$

where $V_{\mathrm{s}}=(\Delta r\tan\varphi)/(KT)$ denotes the search velocity corresponding to the search rotation angle.

Performing FT on Eq. (35) along the fast time axis, we have

$$\begin{aligned} & s_{\mathrm{rot}}\left(f_{\mathrm{r}},m';V_{\mathrm{s}}\right) \\ &= A_{\mathrm{c}}\exp\left[-\mathrm{j}4\pi\frac{f_{\mathrm{r}}}{c}(R_0+V_{\mathrm{e}}m'T)\right] \\ &\quad\cdot\exp\left(\mathrm{j}4\pi\frac{f_{\mathrm{r}}}{c}V_{\mathrm{s}}m'T\right)\exp\left(-\mathrm{j}4\pi\frac{R_0}{\lambda}\right) \\ &\quad\cdot\exp\left(-\mathrm{j}\frac{4\pi}{\lambda}v_0 m'T\right)\exp\left[-\mathrm{j}\frac{2\pi}{\lambda}a(m'T)^2\right]. \end{aligned} \tag{36}$$

From Eq. (36) we can see that the LRT operation can be replaced by the phase compensation in the spatial frequency domain. The compensation function is expressed as

$$H_{\mathrm{vs}}\left(f_{\mathrm{r}},m';V_{\mathrm{s}}\right)=\exp\left(\mathrm{j}4\pi\frac{f_{\mathrm{r}}}{c}V_{\mathrm{s}}m'T\right). \tag{37}$$

When $V_{\mathrm{s}}=V_{\mathrm{e}}$, the linear coupling term between f_{r} and m' will be eliminated and LRM is accordingly removed. Performing IFT on Eq. (36) along the spatial frequency axis, we obtain

$$\begin{aligned} & s_{\mathrm{rot}}\left(n',m';V_{\mathrm{e}}\right) \\ &= A_{\mathrm{c}}\,\mathrm{sinc}\left[\frac{1}{K}\left(n'-n_{R_0}\right)\right]\exp\left(-\mathrm{j}\frac{2\pi c}{\lambda KB}n_{R_0}\right) \\ &\quad\cdot\exp\left(-\mathrm{j}\frac{4\pi}{\lambda}v_0 m'T\right)\exp\left[-\mathrm{j}\frac{2\pi}{\lambda}a(m'T)^2\right]. \end{aligned} \tag{38}$$

Notably, the velocity search interval should be smaller than $\Delta v=\lambda/(2N_{\mathrm{a}}T)$ according to the Doppler frequency resolution.

Remark 3 Rotation angle search is equivalent to velocity search. The interpolation can be replaced by FT, phase compensation, and IFT, which avoid the numerical errors. In addition, velocity search is more intuitive than rotation angle search, and the result is a natural expression of motion parameters. As to the search interval, the uniform sampling in the rotation angle corresponds to the non-uniform sampling in velocity, which are approximately the same at small angles but have significant differences at large angles.

4.3 Computational cost analysis

In this subsection, computational cost of the proposed LRT-NuFFT will be analyzed in detail. The representative MART-LVT, KT-LVD, TDST, SAF-SFT, and MLRT methods are selected for comparison.

Suppose that N_{φ}, N_{KT}, N_{r}, and N_{a} represent the numbers of search angles, search fold factors, range cells, and pulses, respectively. When the velocity search interval equals the velocity resolution, we have $N_{\varphi}=N_{\mathrm{KT}}N_{\mathrm{a}}$.

Main steps in MART-LVT are the MART operation $O(N_{\mathrm{KT}}N_{\mathrm{a}}N_{\mathrm{r}})$ and LVT operation $O(3N_{\mathrm{a}}^2\log_2 N_{\mathrm{a}})$ (Lv et al., 2011). Thus, the total computational complexity is on the order of $O(3N_{\mathrm{KT}}N_{\mathrm{r}}N_{\mathrm{a}}^3\log_2 N_{\mathrm{a}})$.

As for the KT-LVD method, its main steps contain fold factor search operation $O(N_{\mathrm{KT}}N_{\mathrm{r}})$ and LVD operation $O(3N_{\mathrm{a}}^2\log_2 N_{\mathrm{a}})$ for each range cell. Therefore, the computational cost of KT-LVD is about $O(3N_{\mathrm{KT}}N_{\mathrm{r}}N_{\mathrm{a}}^2\log_2 N_{\mathrm{a}})$.

For TDST, $O(3N_{\mathrm{r}}N_{\mathrm{a}}^2\log_2 N_{\mathrm{a}})$ and $O(3N_{\mathrm{a}}^2N_{\mathrm{r}}\log_2 N_{\mathrm{r}})$ are needed to perform two steps of the scaled Fourier transform (SFT). Thus, the total computational complexity is on the order of $O(3N_{\mathrm{r}}N_{\mathrm{a}}^2\log_2(N_{\mathrm{a}}N_{\mathrm{r}}))$.

The main steps of SAF-SFT include the two steps of SFT, whose computational complexities are $O(3N_{\mathrm{a}}N_{\mathrm{r}}\log_2 N_{\mathrm{a}})$ and $O(3N_{\mathrm{a}}^2\log_2 N_{\mathrm{a}})$. Hence, its computational cost is on the order of $O(3N_{\mathrm{a}}(N_{\mathrm{a}}+N_{\mathrm{r}})\log_2 N_{\mathrm{a}})$.

It is easy to find that the computational cost of MLRT is on the order of $O(N_{\mathrm{KT}}N_{\mathrm{r}}N_{\mathrm{a}}^2\log_2 N_{\mathrm{a}})$.

Different from MART-LVT, phase compensation and NuFFT are used to decrease the computational burden, where the computational cost of an N-point

NuFFT is $O(2N\log_2 N)$. Thus, the overall computational cost of LRT-NuFFT is about $O(2N_{\mathrm{KT}}N_{\mathrm{r}}N_{\mathrm{a}}^2\log_2 N_{\mathrm{a}})$.

Computational complexities of the above methods are listed in Table 1. Under the assumption that N_{r}=N_{a} and N_{KT}=10, Fig. 2 intuitively presents the computational cost curves. It is obvious that the LRT-NuFFT method has much lower computational complexity than MART-LVT and KT-LVD, but higher computational cost than TDST, MLRT, and SAF-SFT. However, when considering the detection performance, the proposed method has great advantages in a low-SNR environment.

Table 1 Computational complexity of different methods

Method	Computational complexity
MART-LVT	$O(3N_{\mathrm{KT}}N_{\mathrm{r}}N_{\mathrm{a}}^3\log_2 N_{\mathrm{a}})$
KT-LVD	$O(3N_{\mathrm{KT}}N_{\mathrm{r}}N_{\mathrm{a}}^2\log_2 N_{\mathrm{a}})$
SAF-SFT	$O(3N_{\mathrm{a}}(N_{\mathrm{a}}+N_{\mathrm{r}})\log_2 N_{\mathrm{a}})$
TDST	$O(3N_{\mathrm{r}}N_{\mathrm{a}}^2\log_2(N_{\mathrm{a}}N_{\mathrm{r}}))$
MLRT	$O(N_{\mathrm{KT}}N_{\mathrm{r}}N_{\mathrm{a}}^2\log_2 N_{\mathrm{a}})$
Ours	$O(2N_{\mathrm{KT}}N_{\mathrm{r}}N_{\mathrm{a}}^2\log_2 N_{\mathrm{a}})$

N_{KT}, N_{r}, and N_{a} represent the numbers of search fold factors, range cells, and pulses, respectively

Table 2 Radar parameters in the simulations

Parameter	Value	Parameter	Value
Carrier frequency (GHz)	1	Bandwidth (MHz)	20
Sample frequency (MHz)	30	Pulse width (μs)	10
PRF (Hz)	256	Number of pulses	512

PRF: pulse repetition frequency

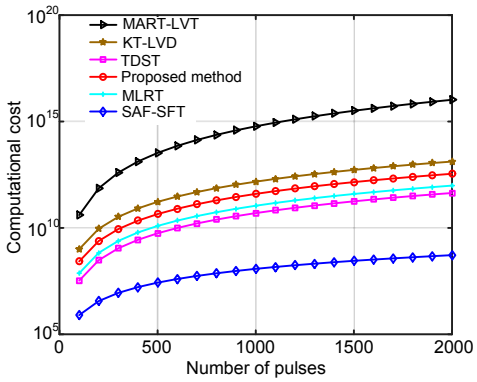

Fig. 2 Comparison results of computational complexity

5 Simulations and real-data processing results

5.1 Coherent integration ability

Radar parameters in the simulations are given in Table 2.

A single maneuvering target is used to evaluate the coherent integration ability of the proposed method. Motion parameters of the target are as follows: R_0=150 km, v=150 m/s, and a=8 m/s^2. Fig. 3a shows the results of the pulse compression with an SNR being −10 dB. It is obvious that the target trajectory is submerged by the serious noise and that no target can be observed. Fig. 3b shows the integration

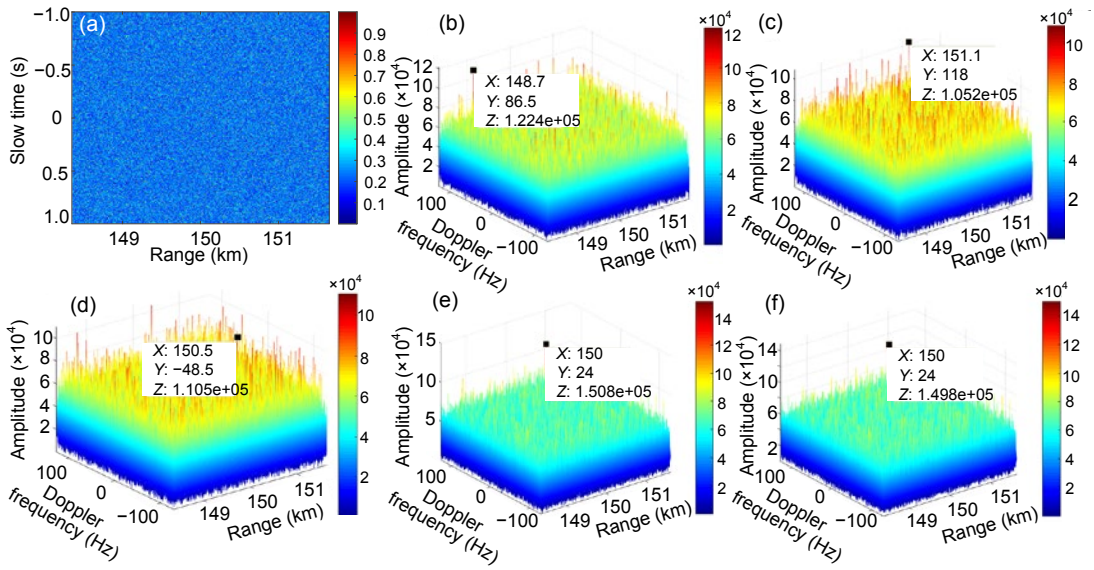

Fig. 3 Coherent integration simulation results of a maneuvering target: (a) pulse compression; (b) MLRT; (c) SAF-SFT; (d) TDST; (e) MART-LVT; (f) LRT-NuFFT

results of MLRT. Without eliminating the effects of QRM and DFM, MLRT fails in detecting the maneuvering target. Figs. 3c and 3d present the integration results of SAF-SFT and TDST, respectively. As the bilinear operation sacrifices some target energy, their outputs are still buried in the noise. For comparison, MART-LVT and LRT-NuFFT integrate the target as a peak at the expected position of the range–Doppler frequency domain (Figs. 3e and 3f). Experimental results demonstrate the integration capability of the proposed method with a low SNR.

In the simulations, the integration performances of two targets are analyzed. Motion parameters of the two targets (Tr1 and Tr2) are given in Table 3. Fig. 4a shows the results of pulse compression. Fig. 4b shows the velocity search results, where two obvious peaks indicate the equivalent velocities of Tr1 and Tr2. Thus, the velocities of Tr1 and Tr2 are estimated as $\hat{v}_{\mathrm{Tr1}}=150$ m/s and $\hat{v}_{\mathrm{Tr2}}=-200$ m/s, respectively. With the corresponding velocity, LRMs of Tr1 and Tr2 are corrected, as shown in Figs. 4c and 4d, respectively. Via NuFFT, accelerations of Tr1 and Tr2 are estimated at the corresponding range cells, i.e., $\hat{a}_{\mathrm{Tr1}}=7.95\ \mathrm{m/s^2}$ and $\hat{a}_{\mathrm{Tr2}}=-4.05\ \mathrm{m/s^2}$, as shown in Figs. 4e and 4f, respectively. Figs. 4g and 4h show the integration results of the two targets. Simulation results demonstrate the integration capability of the proposed method for multiple targets.

Table 3 Parameters of two maneuvering targets in the simulations

Target	SNR (dB)	Initial slant range (km)	Velocity (m/s)	Acceleration ($\mathrm{m/s^2}$)
Tr1	10	150.0	150	8
Tr2	10	150.2	−200	−4

SNR: signal-to-noise ratio

Note that there are several false peaks in Fig. 4b and that the interval between these peaks is exactly half of the blind speed. Thus, denote these false peaks as half-blind-speed sidelobes (HBSSLs). The internal cause of the HBSSLs is analyzed in the Appendix. In real applications, weak targets may be submerged in the HBSSLs caused by strong targets. Therefore, the CLEAN technique (Li et al., 2016b) is suggested.

5.2 Detection performance

We evaluate the detection performance of the proposed method via Monte-Carlo trials. Complex white Gaussian noise with zero mean is added to the signal after pulse compression to yield SNRs varying from −25 dB to 5 dB. SNR is defined as

$$\mathrm{SNR}=10\lg\frac{A_{\mathrm{c}}^2}{\sigma^2}, \tag{39}$$

where σ^2 is the variance of the Gaussian noise.

For each SNR, 500 independent simulations are performed. The false alarm ratio is set as $P_{\mathrm{fa}}=10^{-6}$. Five representative coherent integration methods, i.e., MART-LVT, KT-LVD, TDST, SAF-SFT, and MLRT, are selected for comparison.

Detection probability curves are shown in Fig. 5. It is clear that LRT-NuFFT obtains nearly the same detection ability as the ideal processing, because LRT-NuFFT effectively eliminates the effects of LRM, QRM, and DFM and realizes coherent integration of the target energy. MART-LVT and KT-LVD suffer from some integration performance losses because they ignore the QRM effects caused by the target's acceleration. SNRs for TDST and SAF-SFT are 3 dB and 6 dB higher than those of the ideal situation, respectively, indicating that the bilinear operations lose much signal energy and deteriorate the anti-noise performance. As expected, the detection performance of MLRT is poor due to its poor ability to deal with the effects of QRM and DFM.

5.3 Real-data processing results

In this subsection, we adopt the measured data of a DJI Phantom 3 commercial UAV to demonstrate the proposed method. The data was collected in March 2017 by the National University of Defense Technology, Hunan Province, China. Figs. 6a and 6b present the experimental scene and frequency modulated continuous wave (FMCW) radar system, respectively. Radar parameters are given in Table 4. Note that to obtain LRM and Doppler ambiguity, we artificially enlarge the bandwidth and reduce PRF.

Fig. 6c shows the target trajectory after pulse compression. The coherent time is 0.92 s, during which the UAV moves across several range cells and causes serious range migration. Fig. 6d shows the equivalent velocity estimation results. The velocity search scope is set as [−10, 10] m/s, and the search interval is 0.01 m/s. From the peak position, we can

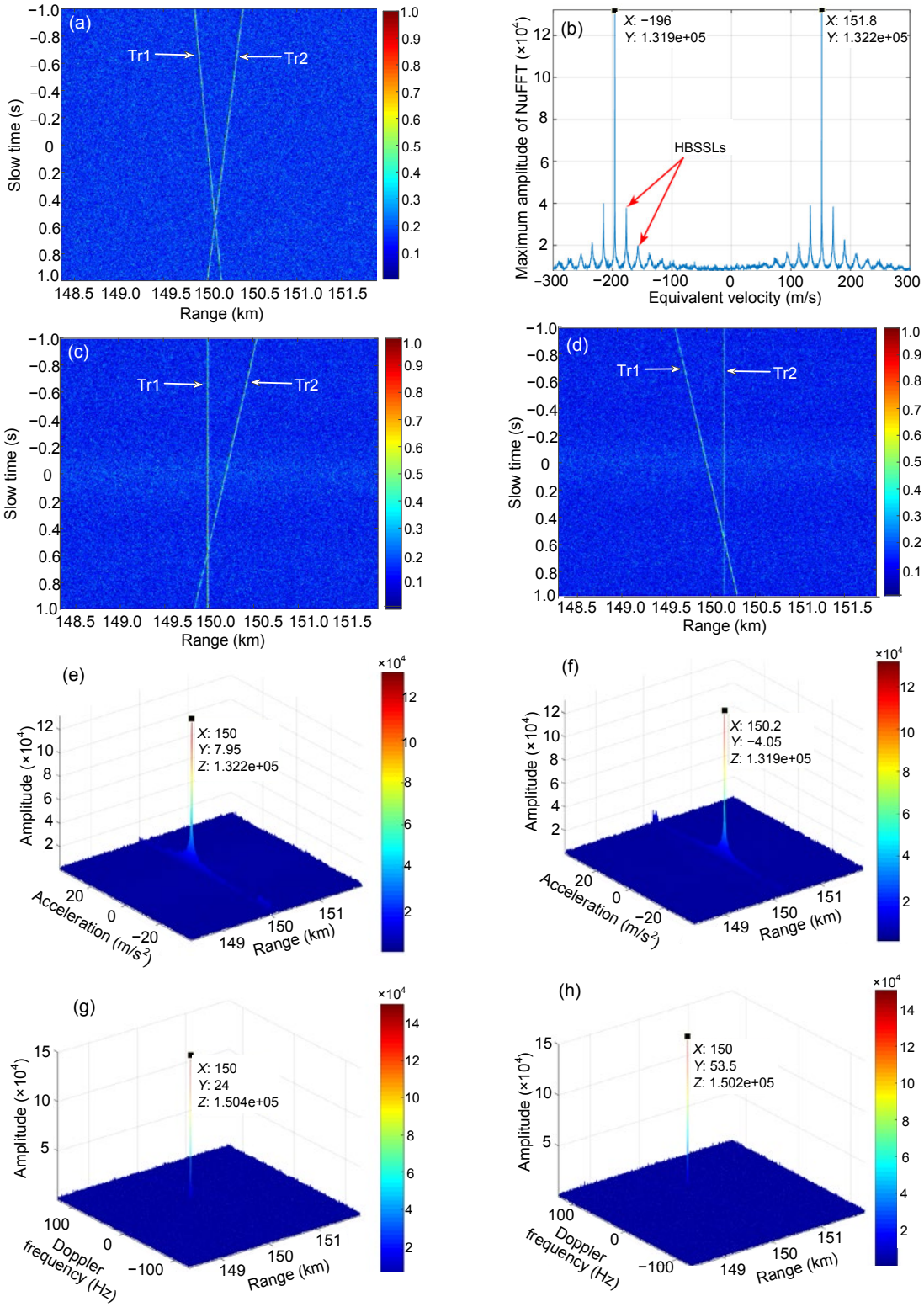

Fig. 4 Coherent integration simulation results of LRT-NuFFT for multiple targets

(a) results of pulse compression; (b) equivalent velocity search results; (c) range migration correction results of Tr1; (d) range migration correction results of Tr2; (e) acceleration estimation results of Tr1; (f) acceleration estimation results of Tr2; (g) integration results of Tr1; (h) integration results of Tr2

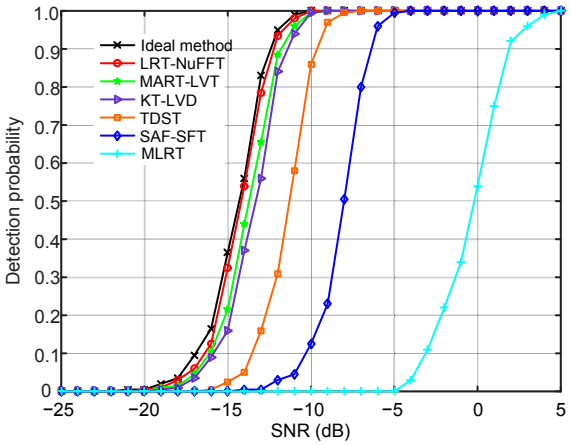

Fig. 5 Detection probability against the signal-to-noise ratio (SNR)

estimate the equivalent velocity and true velocity of the target to be $\hat{V}_e = 1$ m/s and $\hat{v} = 1.2105$ m/s, respectively. After phase compensation, LRM is corrected (Fig. 6e) and the acceleration of the UAV is obtained via NuFFT (Fig. 6f), i.e., $\hat{a} = 0.2231\,\mathrm{m/s^2}$.

Table 4 Frequency modulated continuous wave radar parameters

Parameter	Value	Parameter	Value
Carrier frequency (GHz)	9.5	PRF (Hz)	50
Bandwidth (GHz)	1	Sampling frequency (MHz)	1
Pulse width (s)	0.0102	Coherent time (s)	0.92

PRF: pulse repetition frequency

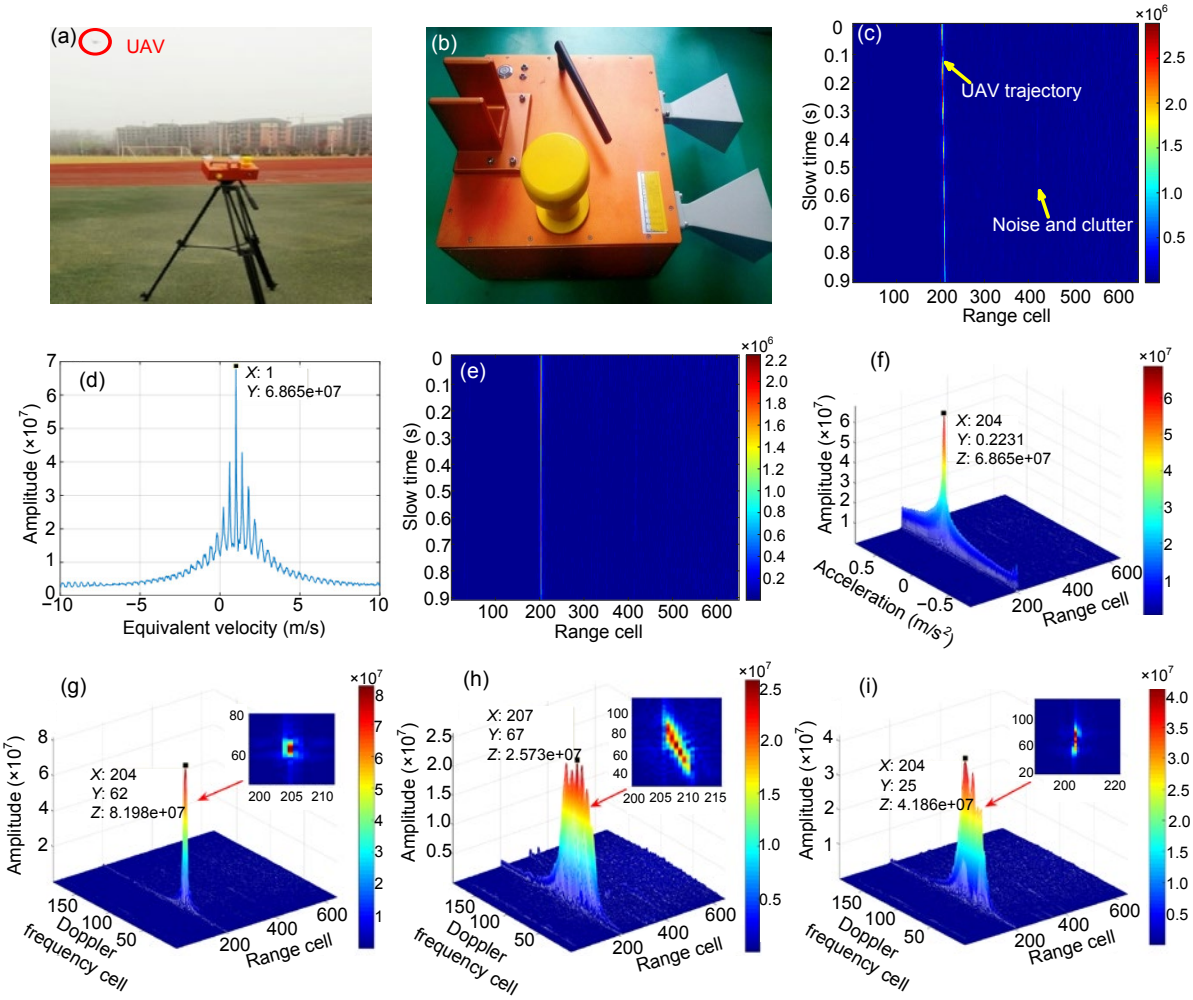

Fig. 6 Processing results with real data

(a) experimental scene; (b) frequency modulated continuous wave radar system; (c) results of pulse compression; (d) equivalent velocity estimation results; (e) results of LRM correction; (f) acceleration estimation results of NuFFT; (g) integration results of LRT-NuFFT; (h) integration results of MTD; (i) integration results of MLRT

Fig. 6g depicts the coherent integration results of LRT-NuFFT, where a well-focused peak is observed in the range–Doppler frequency domain. At the same time, the integration results of MTD and MLRT are presented for comparison in Figs. 6h and 6i, respectively. However, the target energy is dispersed over multiple range cells and velocity cells, which creates difficulties for target detection.

6 Conclusions

In this study, we have proposed a novel fast method based on LRT and NuFFT for maneuvering target detection. The effects of LRM, QRM, and DFM have been eliminated via LRT, SoKT, and NuFFT, respectively. At the same time, an equivalent velocity search method has been derived to avoid interpolation. Simulation results showed that the proposed LRT-NuFFT method could achieve nearly ideal detection performance at low computational cost. Experimental results from UAV echoes demonstrated the effectiveness of the proposed method.

Contributors

Ke JIN designed the research and drafted the manuscript. Tao LAI and Yan-li QI processed the data. Jie HUANG and Yong-jun ZHAO helped organize the manuscript. Ke JIN and Tao LAI revised and finalized the paper.

Compliance with ethics guidelines

Ke JIN, Tao LAI, Yan-li QI, Jie HUANG, and Yong-jun ZHAO declare that they have no conflict of interest.

References

Chen XL, Guan J, Liu NB, et al., 2014. Maneuvering target detection via Radon-fractional Fourier transform-based long-time coherent integration. *IEEE Trans Signal Process*, 62(4):939-953. https://doi.org/10.1109/TSP.2013.2297682

Guida M, Longo M, Lops M, 1993. Biparametric CFAR procedures for lognormal clutter. *IEEE Trans Aerosp Electron Syst*, 29(3):798-809. https://doi.org/10.1109/7.220931

Huang PH, Liao GS, Yang ZZ, et al., 2016. Long-time coherent integration for weak maneuvering target detection and high-order motion parameter estimation based on keystone transform. *IEEE Trans Signal Process*, 64(15): 4013-4026. https://doi.org/10.1109/TSP.2016.2558161

Huang X, Zhang LR, Li SY, et al., 2018. Radar high speed small target detection based on keystone transform and linear canonical transform. *Dig Signal Process*, 82:203-215. https://doi.org/10.1016/j.dsp.2018.08.001

Huang X, Tang SY, Zhang LR, et al., 2019. Ground-based radar detection for high-speed maneuvering target via fast discrete chirp-Fourier transform. *IEEE Access*, 7:12097-12113. https://doi.org/10.1109/ACCESS.2019.2892505

Jin K, Lai T, Li GQ, et al., 2017. Ultra-wideband FMCW ISAR imaging with a large rotation angle based on block-sparse recovery. *Front Inform Technol Electron Eng*, 18(12): 2058-2069. https://doi.org/10.1631/FITEE.1601310

Jin K, Lai T, Wang YB, et al., 2019a. Coherent integration for radar high-speed maneuvering target based on frequency-domain second-order phase difference. *Electronics*, 8(3): 287. https://doi.org/10.3390/electronics8030287

Jin K, Lai T, Wang YB, et al., 2019b. Parameter estimation of quadratic frequency modulated signal based on three-dimensional scaled Fourier transform. *IET Radar Sonar Navig*, 13(10):1689-1696. https://doi.org/10.1049/iet-rsn.2018.5530

Kirkland D, 2011. Imaging moving targets using the second-order keystone transform. *IET Radar Sonar Navig*, 5(8): 902-910. https://doi.org/10.1049/iet-rsn.2010.0304

Li XL, Cui GL, Yi W, et al., 2014. A fast maneuvering target motion parameters estimation algorithm based on ACCF. *IEEE Signal Process Lett*, 22(3):270-274. https://doi.org/10.1109/LSP.2014.2358230

Li XL, Cui GL, Yi W, et al., 2015. Coherent integration for maneuvering target detection based on Radon-Lv's distribution. *IEEE Signal Process Lett*, 22(9):1467-1471. https://doi.org/10.1109/LSP.2015.2390777

Li XL, Cui GL, Yi W, et al., 2016a. Manoeuvring target detection based on keystone transform and Lv's distribution. *IET Radar Sonar Navig*, 10(7):1234-1242. https://doi.org/10.1049/iet-rsn.2015.0488

Li XL, Kong LJ, Cui GL, et al., 2016b. CLEAN-based coherent integration method for high-speed multi-targets detection. *IET Radar Sonar Navig*, 10(9):1671-1682. https://doi.org/10.1049/iet-rsn.2015.0653

Li XL, Cui GL, Yi W, et al., 2016c. Fast coherent integration for maneuvering target with high-order range migration via TRT-SKT-LVD. *IEEE Trans Aerosp Electron Syst*, 52(6):2803-2814. https://doi.org/10.1109/taes.2016.150573

Li XL, Cui GL, Kong LJ, et al., 2016d. Fast non-searching method for maneuvering target detection and motion parameters estimation. *IEEE Trans Signal Process*, 64(9): 2232-2244. https://doi.org/10.1109/TSP.2016.2515066

Li XL, Kong LJ, Cui GL, et al., 2016e. A low complexity coherent integration method for maneuvering target detection. *Dig Signal Process*, 52:137-147. https://doi.org/10.1016/j.dsp.2015.10.008

Li XL, Sun Z, Yi W, et al., 2018. Computationally efficient coherent detection and parameter estimation algorithm for maneuvering target. *Signal Process*, 155:130-142. https://doi.org/10.1016/j.sigpro.2018.09.030

Li XL, Sun Z, Yi W, et al., 2019a. Radar detection and parameter estimation of high-speed target based on MART-

LVT. *IEEE Sens J*, 19(4):1478-1486. https://doi.org/10.1109/JSEN.2018.2882198

Li XL, Sun Z, Yeo TS, et al., 2019b. STGRFT for detection of maneuvering weak target with multiple motion models. *IEEE Trans Signal Process*, 67(7):1902-1917. https://doi.org/10.1109/TSP.2019.2899318

Luo S, Bi GA, Lv XL, et al., 2013. Performance analysis on Lv distribution and its applications. *Dig Signal Process*, 23(3):797-807. https://doi.org/10.1016/j.dsp.2012.11.011

Lv XL, Bi GA, Wan CR, et al., 2011. Lv's distribution: principle, implementation, properties, and performance. *IEEE Trans Signal Process*, 59(8):3576-3591. https://doi.org/10.1109/TSP.2011.2155651

Niu ZY, Zheng JB, Su T, et al., 2017. Fast implementation of scaled inverse Fourier transform for high-speed radar target detection. *Electron Lett*, 53(16):1142-1144. https://doi.org/10.1049/el.2017.1782

Perry RP, Dipietro F, Fante RL, 1999. SAR imaging of moving targets. *IEEE Trans Aerosp Electron Syst*, 35(1):188-200. https://doi.org/10.1109/7.745691

Pignol F, Colone F, Martelli T, 2018. Lagrange-polynomial-interpolation-based keystone transform for a passive radar. *IEEE Trans Aerosp Electron Syst*, 54(3):1151-1167. https://doi.org/10.1109/TAES.2017.2775924

Qu ZY, Qu FX, Hou CB, et al., 2018. Quadratic frequency modulation signals parameter estimation based on two-dimensional product modified parameterized chirp rate-quadratic chirp rate distribution. *Sensors*, 18(5):1624. https://doi.org/10.3390/s18051624

Rao X, Tao HH, Su J, et al., 2014. Axis rotation MTD algorithm for weak target detection. *Dig Signal Process*, 26:81-86. https://doi.org/10.1016/j.dsp.2013.12.003

Rao X, Tao HH, Su J, et al., 2015. Detection of constant radial acceleration weak target via IAR-FRFT. *IEEE Trans Aerosp Electron Syst*, 51(4):3242-3253. https://doi.org/10.1109/TAES.2015.140739

Su J, Xing M, Wang G, et al., 2010. High-speed multi-target detection with narrowband radar. *IET Radar Sonar Navig*, 4(4):595-603. https://doi.org/10.1049/iet-rsn.2008.0160

Sun Z, Li XL, Yi W, et al., 2018. A coherent detection and velocity estimation algorithm for the high-speed target based on the modified location rotation transform. *IEEE J Sel Top Appl Earth Observ Remote Sens*, 11(7):2346-2361. https://doi.org/10.1109/JSTARS.2018.2834535

Tian J, Cui W, Shen Q, et al., 2013. High-speed maneuvering target detection approach based on joint RFT and keystone transform. *Sci China Inform Sci*, 56(6):1-13. https://doi.org/10.1007/s11432-013-4880-z

Tian J, Cui W, Wu S, 2014. A novel method for parameter estimation of space moving targets. *IEEE Geosci Remote Sens Lett*, 11(2):389-393. https://doi.org/10.1109/LGRS.2013.2263332

Wu W, Wang GH, Sun JP, 2018. Polynomial Radon-polynomial Fourier transform for near space hypersonic maneuvering target detection. *IEEE Trans Aerosp Electron Syst*, 54(3):1306-1322. https://doi.org/10.1109/TAES.2017.2780658

Xing MD, Su JH, Wang GY, et al., 2011. New parameter estimation and detection algorithm for high speed small target. *IEEE Trans Aerosp Electron Syst*, 47(1):214-224. https://doi.org/10.1109/TAES.2011.5705671

Xu J, Yu J, Peng YN, et al., 2011a. Radon-Fourier transform for radar target detection, I: generalized Doppler filter bank. *IEEE Trans Aerosp Electron Syst*, 47(2):1186-1202. https://doi.org/10.1109/TAES.2011.5751251

Xu J, Yu J, Peng YN, et al., 2011b. Radon-Fourier transform for radar target detection (II): blind speed sidelobe suppression. *IEEE Trans Aerosp Electron Syst*, 47(4):2473-2489. https://doi.org/10.1109/TAES.2011.6034645

Xu J, Xia XG, Peng SB, et al., 2012. Radar maneuvering target motion estimation based on generalized Radon-Fourier transform. *IEEE Trans Signal Process*, 60(12):6190-6201. https://doi.org/10.1109/TSP.2012.2217137

Yu J, Xu J, Peng YN, et al., 2012. Radon-Fourier transform for radar target detection (III): optimality and fast implementations. *IEEE Trans Aerosp Electron Syst*, 48(2):991-1004. https://doi.org/10.1109/taes.2012.6178044

Zhang JC, Su T, Zheng JB, et al., 2017. Novel fast coherent detection algorithm for radar maneuvering target with jerk motion. *IEEE J Sel Top Appl Earth Observ Remote Sens*, 10(5):1792-1803. https://doi.org/10.1109/JSTARS.2017.2651156

Zheng JB, Su T, Zhang L, et al., 2014. ISAR imaging of targets with complex motion based on the chirp rate-quadratic chirp rate distribution. *IEEE Trans Geosci Remote Sens*, 52(11):7276-7289. https://doi.org/10.1109/tgrs.2014.2310474

Zheng JB, Su T, Zhu WT, et al., 2015. Radar high-speed target detection based on the scaled inverse Fourier transform. *IEEE J Sel Top Appl Earth Observ Remote Sens*, 8(3):1108-1119. https://doi.org/10.1109/JSTARS.2014.2368174

Zheng JB, Liu HW, Liu J, et al., 2018. Radar high-speed maneuvering target detection based on three-dimensional scaled transform. *IEEE J Sel Top Appl Earth Observ Remote Sens*, 11(8):2821-2833. https://doi.org/10.1109/JSTARS.2018.2846731

Zhu DY, Li Y, Zhu ZD, 2007. A keystone transform without interpolation for SAR ground moving-target imaging. *IEEE Geosci Remote Sens Lett*, 4(1):18-22. https://doi.org/10.1109/LGRS.2006.882147

Zhu SQ, Liao GS, Yang D, et al., 2014. A new method for radar high-speed maneuvering weak target detection and imaging. *IEEE Geosci Remote Sens Lett*, 11(7):1175-1179. https://doi.org/10.1109/LGRS.2013.2283887

Appendix: Derivation of HBSSLs

Because of the discrete pulse sampling, finite range resolution, and limited integration time, HBSSLs will inevitably appear. When deriving the HBSSLs of LRT-NuFFT, we may refer to the blind speed sidelobes (BSSLs) of RFT (Xu et al., 2011b).

Assume that VS-NuFFT is used to achieve the LRT operation. Consider the discrete form of Eq. (35) as

$$\begin{aligned} & s_{\mathrm{rot}}\left(n',m';V_{\mathrm{s}}\right) \\ &= A_{\mathrm{c}}\exp\left(-\mathrm{j}\frac{2\pi c}{\lambda KB}n_{R_0}\right)\exp\left(-\mathrm{j}\frac{4\pi}{\lambda}q_{\mathrm{b}}\Delta v m'T\right) \\ &\quad\cdot\exp\left(-\mathrm{j}\frac{2\pi}{\lambda}a(m'T)^2\right)\mathrm{sinc}\left[\frac{\rho_{\mathrm{r}}}{\Delta r}\left(n'-n_{R_0}\right)\right. \\ &\quad\left.+\frac{m'T}{\Delta r}(s-N_{\mathrm{b}})v_{\mathrm{b}}+\frac{m'T}{\Delta r}\left(q_{\mathrm{s}}-\frac{q_{\mathrm{b}}}{2}\right)\Delta v\right], \end{aligned} \tag{A1}$$

where $V_{\mathrm{s}}=sv_{\mathrm{b}}+q_{\mathrm{s}}\Delta v$, $V_{\mathrm{e}}=N_{\mathrm{b}}v_{\mathrm{b}}+q_{\mathrm{b}}\Delta v/2$, $v_0=q_{\mathrm{b}}\Delta v$, and $s=\mathrm{round}(V_{\mathrm{s}}/v_{\mathrm{b}})$ (round(·) denotes the round up operation).

The phase compensation function in Eq. (22) can be written as

$$H_1(m')=\exp\left(\mathrm{j}\frac{4\pi}{\lambda}2q_{\mathrm{s}}\Delta v m'T\right). \tag{A2}$$

Multiplying Eq. (A2) with Eq. (A1) and performing NuFFT to accumulate target energy, we have Eq. (A3), which is expressed at the bottom of this page.

To simplify the derivation, only $f_{(m'T)^2}=-a/\lambda$ is considered. When $f_{(m'T)^2}\neq -a/\lambda$, the second-order terms of mT' defocus the target energy, and thus cannot form a sharp peak. Consequently, Eq. (A3) is simplified as

$$\begin{aligned} s_{\mathrm{NuFFT}}(n',s) &= \sum_{m'=-N_a/2}^{N_a/2-1} A_{\mathrm{c}}\exp\left(-\mathrm{j}\frac{2\pi c}{\lambda KB}n_{R_0}\right) \\ &\quad\cdot\exp\left[\mathrm{j}\frac{4\pi}{\lambda}\left(2q_{\mathrm{s}}-q_{\mathrm{b}}\right)\Delta v m'T\right] \\ &\quad\cdot\mathrm{sinc}\left[\frac{\rho_{\mathrm{r}}}{\Delta r}\left(n'-n_{R_0}\right)+\frac{m'T}{\Delta r}(s-N_{\mathrm{b}})v_{\mathrm{b}}\right. \\ &\quad\left.+\frac{m'T}{\Delta r}\left(q_{\mathrm{s}}-\frac{q_{\mathrm{b}}}{2}\right)\Delta v\right]. \end{aligned} \tag{A4}$$

It is easy to see that Eq. (A4) is the derivation of the BSSLs in RFT. We may refer to the results of RFT (Xu et al., 2011b) and directly give the result, i.e.,

$$s_{\mathrm{NuFFT}}(n',s)\approx I_0+\sum_{p=1,p\neq s} I_p, \tag{A5}$$

where

$$I_0=A_{\mathrm{c}}N_{\mathrm{a}}\,\mathrm{sinc}\left[\frac{\rho_{\mathrm{r}}}{\Delta r}\left(n'-n_{R_0}\right)\right]\delta\left(q_{\mathrm{s}}-\frac{q_{\mathrm{b}}}{2}\right), \tag{A6}$$

$$\begin{aligned} I_{\mathrm{p}} &= \frac{A_{\mathrm{c}}f_{\mathrm{p}}\Delta r}{(s-N_{\mathrm{b}})v_{\mathrm{b}}}\mathrm{rect}\left[\frac{\left(n'-n_{R_0}\right)}{(s-N_{\mathrm{b}})v_{\mathrm{b}}T}\Delta r\right] \\ &\quad\cdot\mathrm{sinc}\left[\frac{\Delta r(2q_{\mathrm{s}}-q_{\mathrm{b}})}{v_{\mathrm{b}}T(s-N_{\mathrm{b}})}\right], \end{aligned} \tag{A7}$$

where $f_{\mathrm{p}}=1/T$ denotes the pulse repetition frequency.

It is evident that the response of a single target in the NuFFT domain is composed of one main peak I_0, which indicates the initial range and equivalent

$$\begin{aligned} s_{\mathrm{NuFFT}}\left(n',s,f_{(m'T)^2}\right) &= \mathrm{NuFFT}\left[s_{\mathrm{rot}}(n',m';V_{\mathrm{s}})H_1(m')\right] \\ &= \sum_{m'=-N_a/2}^{N_a/2-1} s_{\mathrm{rot}}(n',m';V_{\mathrm{s}})H_1(m')\exp\left[-\mathrm{j}2\pi f_{(m'T)^2}(m'T)^2\right] \\ &= \sum_{m'=-N_a/2}^{N_a/2-1} A_{\mathrm{c}}\exp\left(-\mathrm{j}\frac{2\pi c}{\lambda KB}n_{R_0}\right)\exp\left[\mathrm{j}\frac{4\pi}{\lambda}(2q_{\mathrm{s}}-q_{\mathrm{b}})\Delta v m'T\right]\exp\left[-\mathrm{j}\frac{2\pi}{\lambda}\left(f_{(m'T)^2}+\frac{a}{\lambda}\right)(m'T)^2\right] \\ &\quad\cdot\mathrm{sinc}\left[\frac{\rho_{\mathrm{r}}}{\Delta r}\left(n'-n_{R_0}\right)+\frac{m'T}{\Delta r}(s-N_{\mathrm{b}})v_{\mathrm{b}}+\frac{m'T}{\Delta r}\left(q_{\mathrm{s}}-\frac{q_{\mathrm{b}}}{2}\right)\Delta v\right]. \end{aligned} \tag{A3}$$

velocity of the target. The interval between the two peaks of I_{p} is half the blind speed. By Eq. (A7), the velocity slice at $n' = n_{R_0}$ is

$$s_{\mathrm{NuFFT}}\left(n_{R_0}, s\right) \approx A_{\mathrm{c}} N_{\mathrm{a}} \delta\left(q_{\mathrm{s}} - \frac{q_{\mathrm{b}}}{2}\right) + \frac{A_{\mathrm{c}} f_{\mathrm{p}} \Delta r}{(s - N_{\mathrm{b}}) v_{\mathrm{b}}} \sum_{p=1, p \neq s} \mathrm{sinc}\left[\frac{\Delta r (2q_{\mathrm{s}} - q_{\mathrm{b}})}{v_{\mathrm{b}} T (s - N_{\mathrm{b}})}\right]. \tag{A8}$$

Eq. (A8) indicates the HBSSLs obtained by the proposed method. When QRM and SoKT are neglected, HBSSLs will become BSSLs.